An Atomic Sensor for Direct Detection of Weak Microwave Signals

Vladislav Gerginov, Fabio C. S. da Silva, *Member, IEEE*, Archita Hati, *Member, IEEE*, and Craig Nelson, *Member, IEEE*

***Abstract*— This paper demonstrates direct detection of weak signals at microwave frequencies based on parametric frequency conversion. The atomic medium is optically pumped by a resonant light field and prepared in a coherent atomic superposition by a weak microwave field. The coherent atomic superposition causes a parametric modulation of the polarization of a probe light field at the microwave field frequency. An upper limit magnetic field component sensitivity of 1.2(1.0) pT/Hz$^{1/2}$, corresponding to 3.7(3.1)-μV/cm/Hz$^{1/2}$ electric field component sensitivity, is achieved at ∼6.835 GHz with a 33-mm^3 vapor cell.**

***Index Terms*— Atomic magnetometer, microwave detection, parametric resonance**

I. Introduction

SOME of the most sensitive sensors of physical quantities are based on atomic spectroscopy. Examples are devices measuring time (atomic clocks), magnetic field (atomic magnetometers), and electric field (Rydberg atoms sensors). Atomic clock accuracies reach 18 digits of precision [1]–[3], enabled through sensitive probing of atomic transitions. Atomic magnetometers have demonstrated subfemtotesla sensitivities measuring both dc [4] and radio frequency (RF) magnetic field amplitudes [5]. Sensors based on Rydberg atoms reach electric field component sensitivities of ∼3 μV/cm/Hz$^{1/2}$ at microwave (GHz) frequencies, with sensitivity projected to reach ∼pV/cm/Hz$^{1/2}$ [6].

The extremely high sensitivity to electric fields of Rydberg atoms makes them the natural choice for measurement and calibration of weak ac electric signals [7], [8] as well as imaging with sub-wavelength resolution [9]–[11]. Sensors detecting the magnetic component of a microwave signal have also been investigated for detection and imaging [12]–[19]. Typically, these sensors are based on microwave-optical double resonance (ODR) in alkali atoms [20]. The accuracy of the microwave power measurement is SI-traceable using the atomic candle method [21]. The sensors measure either a Rabi frequency (values range from ×100 Hz [19] to ×10 kHz [13], [17]) or a Rabi resonance [12], [18]. Microwave frequency sensitivity and tunability is achieved by placing the atoms in a strong bias static magnetic field. The inhomogeneity and noise of the strong bias field lead to resonance broadening that reaches megahertz levels [16].

For reference, the ac magnetic field component sensitivity, equivalent to 1 μV/cm/Hz$^{1/2}$, is 0.33 pT/Hz$^{1/2}$. This level has been exceeded at frequencies below 1 MHz using RF atomic magnetometers [22]. This paper shows that it is possible to configure a setup based on an alkali atom buffer gas vapor cell as a sensor that allows magnetic-component microwave field sensitivities at the 1-pT/Hz$^{1/2}$ level (corresponding to ∼3 μV/cm/Hz$^{1/2}$) to be reached with a direct magnetic-component optical detection of a microwave signal amplitude. This configuration based on a parametric frequency conversion process has been previously studied [23], [24]. The configuration can be considered the microwave-frequency equivalent of the RF atomic magnetometer [22], with the microwave-frequency magnetic field exciting transitions between the hyperfine ground components of an alkali atom, the same way an RF magnetic field excites transitions between the Zeeman states of the same ground state component in an RF atomic magnetometer. The microwave signal is encoded on a property of a probe optical field (in this paper, a probe laser light polarization) that is converted to an electric signal after the state of polarization is analyzed.

The detected signal is at the microwave frequency, providing a coherent microwave phase information that is transferred to the optical domain. Such information is inaccessible using ODR [16] or Rydberg atom spectroscopy based on the splitting of electromagnetically induced transparency resonance [6], since these methods are only sensitive to the power of the microwave field. Coherent microwave-to-optical conversion in cold Rydberg atoms through six-wave mixing has also been demonstrated, but the setup requires laser cooling [25], [26].

The use of a buffer gas vapor cell for microwave signal detection offers several advantages. The experimental setup is simple, as no laser cooling is necessary. The laser linewidth requirements are relaxed since all optical transitions are frequency-broadened due to buffer gas-induced collisions. The sensor developed in this paper is small, simple, and attractive for non-conductive weak microwave signal detection [6], [7] and near-field imaging applications [9], [10], [13], [27].

Manuscript received January 17, 2019; revised May 13, 2019; accepted May 16, 2019. Date of publication July 2, 2019; date of current version August 16, 2019. This research has been funded by the Time and Frequency Division of NIST. *(Corresponding author: Vladislav Gerginov.)*

V. Gerginov is with the National Institute of Standards and Technology, Boulder, CO 80305 USA, and also with the Department of Physics, University of Colorado at Boulder, Boulder, CO 80309 USA (e-mail: vladislav.gerginov@colorado.edu).

F. C. S. da Silva, A. Hati, and C. Nelson are with the Time and Frequency Division, National Institute of Standards and Technology, Boulder, CO 80305 USA (e-mail: fabio.dasilva@nist.gov; archita.hati@nist.gov; craig.nelson@nist.gov).

Color versions of one or more of the figures in this article are available online at http://ieeexplore.ieee.org.

Digital Object Identifier 10.1109/TMTT.2019.2921351

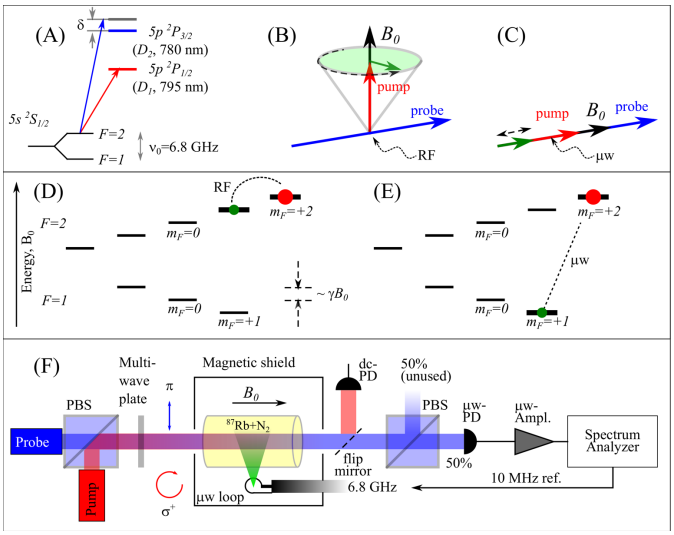

Fig. 1. (A) ^{87}Rb energy diagram (not to scale). (B) Diagram of an RF atomic magnetometer for the detection of weak resonant RF magnetic fields. (C) Diagram for direct detection of weak microwave signals. (D) and (E) Relevant atomic ground states involved in the process of field measurement and their energy/frequency splitting (not to scale) related to (B) and (C). The relevant stretched atomic states are shown with thicker horizontal lines. (F) Experimental setup for direct microwave field detection: PBS—polarizing beam splitter, dc-PD—low-frequency photodiode, μw-PD—fast photodiode, and μw-Ampl—microwave amplifier. The multi-order waveplate keeps the 780-nm probe light linearly polarized and converts the polarization of the 795-nm pump light to circular σ^+. The bias magnetic field B_0 is oriented along the light direction of propagation.

Additionally, because of the direct amplitude detection of the microwave signal, the sensor can be used for communications [28], [29] with modulation schemes that include phase modulation, without the need for laser cooling. Finally, the sensor can be used as a low-power microwave-to-optical converter [26] or a microwave polarization modulator [30].

II. Microwave Coherence Detection

Fig. 1(A) shows a simplified energy diagram of the ^{87}Rb atom and its atomic structure relevant to this paper. The atomic ground state has two hyperfine structure components separated by ~6.8 GHz [31]. The two lowest lying excited states $5p\ ^2P_{1/2}$ and $5p\ ^2P_{3/2}$ can be excited from the ground state $5s\ ^2S_{1/2}$ using resonant light. In this experiment, the $5s\ ^2S_{1/2} \rightarrow 5p\ ^2P_{1/2}$ transition (D_1 transition at 795 nm) is used for optical pumping. The $5s\ ^2S_{1/2} \rightarrow 5p\ ^2P_{3/2}$ transition (D_2 transition at 780 nm) is used for detection of the atomic ground state polarization using polarization rotation measurement of an off-resonant (detuned) probe optical field. The use of independent light fields allows separate optimization of the optical pumping and detection processes.

Fig. 1(D) and (E) shows two relevant atomic ground state diagrams for magnetic field component detection based on optical pumping in a ^{87}Rb atom buffer gas cell. In the presence of a static magnetic field B_0 (defining the atomic quantization axis), the energies of the atomic states belonging to the given ground state components are no longer degenerate.

Fig. 1(B) and (D) shows the detection scheme for measuring RF magnetic fields using a generic RF atomic magnetometer [22]. The RF magnetometer detects RF magnetic field signals that have a frequency within the resonant bandwidth of the magnetometer that is centered at the Larmor frequency $\omega_L = \gamma \times B_0$. In the absence of a resonant magnetic signal, the ground state atomic polarization is oriented along the magnetic field B_0 (and the quantization axis)—for example, by a σ^+ circularly polarized pump light field (not shown). The atoms are in a maximally stretched atomic state, for example, the $F = I + 1/2$, $m_{I+1/2} = +F$ atomic state of the ground state component F that is shown with a long red arrow. Here, F is the total angular momentum and I is the nuclear spin. The orbital angular momentum of the alkali atom ground state, $J = 1/2$, has been considered. When a resonant RF magnetic signal is present, it drives atomic transitions that lead to atomic polarization in the plane orthogonal to the quantization field direction, shown with a short green arrow. The atomic polarization amplitude is a function of the microwave field amplitude. The atomic polarization precesses at the atomic transition frequency in the plane perpendicular to the direction of B_0, as shown by a short green arrow. Its rotation around the direction of B_0 is shown with a dashed arc. The precessing atomic polarization leads to polarization rotation of the probe light field through the Faraday effect [32].

Fig. 1(C) and (E) shows the detection scheme for measuring microwave-frequency magnetic fields and is the subject of this paper. Initially, the atoms are optically pumped into a maximally stretched state of one of the ground state components, for example, in the $F = I + 1/2$, $m_{I+1/2} = +F$ atomic level, shown with a long red arrow, by a σ^+ circularly polarized pump light field (not shown). The interaction with the resonant microwave field prepares the atoms in a coherent hyperfine superposition (or coherence) of the two maximally stretched ground states $F = I + 1/2$, $m_{I+1/2} = +F$ and $F = I - 1/2$, $m_{I-1/2} = +F$ (the latter shown with a short green arrow) along the direction of B_0. As in the case of Fig. 1(B), the transition probability is a function of the microwave amplitude (continuous-wave (CW) regime) or the microwave pulse area (pulsed regime). Since all other atomic transitions are detuned from resonance, the microwave transition $|2, +2\rangle \rightarrow |1, +1\rangle$ can be considered a two-level system that will exhibit Rabi oscillations as a function of the microwave amplitude or pulse area.

If we ignore the nonlinear Zeeman effect, the atomic hyperfine coherence will oscillate at a frequency $\omega = \omega_{\mathrm{HFS}} + (m_{I+1/2} + m_{I-1/2})\gamma \times B$ with $\omega_{\mathrm{HFS}} = 2\pi\nu_0$, the angular frequency corresponding to the unperturbed ground state hyperfine frequency interval ν_0, shown in Fig. 1(E) with a dashed arrow. The oscillating hyperfine coherence is related to the susceptibility of the atomic medium and will affect the properties of a light field propagating through it [33]. Here, a probe light field is considered with optical frequency that is far-detuned from a given atomic transition that involves the atomic ground state and its coherences. The detuning is large compared to the atomic hyperfine structure frequency interval of both the excited and the ground states and the pressure-broadened linewidth of the optical atomic transition. The magnitude of the polarization rotation of such light field will depend on the field's frequency detuning from the atomic

transition and will be modulated at the atomic frequency ω due to the presence of hyperfine coherences created by the microwave field. The process can be described as a parametric frequency conversion with the coherently prepared medium generating optical sidebands of the probe light field that are orthogonally polarized with respect to the carrier [33]. An intuitive interpretation of the process is that atoms aligned in the stretched state of either the $F = 2$ or $F = 1$ ground state components will cause different angles of the probe field polarization rotation. A coherent superposition of these stretched states will thus lead to a polarization rotation angle that oscillates at the frequency of the hyperfine coherence due to the Faraday effect [32].

Direct detection of an atomic superposition of states belonging to different ground state components in alkali atoms was performed more than 50 years ago [23], [24]. These works showed that the presence of coherently prepared atomic medium modulated the properties of a weak beam passing through it through a parametric frequency conversion process [33], [34]. Almost at the same time, it was suggested that the high atomic sensitivity to microwave fields could be used for the detection of weak microwave signals, with the atoms acting as a microwave-to-optical converter with a noise floor limited by the optical detection of the microwave-frequency modulation of the light [35]. The microwave detection scheme [Fig. 1(B)] used in this paper is closely related to these proof-of-principle experiments. It is also related to ODR measurements used in optically pumped microwave atomic clocks [20], to coherent population trapping (CPT)-based microwave clocks with polarization detection [36], [37], and to hyperfine atomic magnetometers and gradiometers [38]–[40].

In the ODR resonance case, the atoms are optically pumped in a chosen atomic state (for example, the stretched $F = I + 1/2, m_{I+1/2} = +F$ atomic state) by a circularly polarized light field tuned in the vicinity of an atomic transition that leads to reduced pump light absorption. When a resonant microwave field is applied, it transfers the atomic population to atomic levels that increase the pump light absorption [20], [38], [39]. The same change in the pump light absorption takes place in the detection scheme shown in Fig. 1(C) and is used in this paper for ODR detection of microwave signals.

III. Experimental Setup

The experimental configuration for microwave magnetic detection is shown in Fig. 1(F). The setup is based on an enriched ^{87}Rb buffer gas cell described in [41]. The cylindrical cell (inner diameter $D \sim 3.3$ mm and length $L \sim 3.8$ mm, respectively) is filled with 66.7(1.3) kPa (500(10) torr) nitrogen acting as buffer gas and heated to ~90 °C (363 K) with a non-magnetic heater. The cell is placed inside a cylindrical magnetic shield chamber with one end left open. A linearly polarized CW probe beam with 780.117(1)-nm wavelength in vacuum, 14.20(1)-mW optical power, and ~3-mm flat-top diameter propagates along the axis of the vapor cell. The probe beam is blue-detuned by 64.8(0.5) GHz from the pressure-broadened D_2 atomic transition in ^{87}Rb [see Fig. 1(A)] [42], [43]. The probe detuning is significantly larger than the pressure-broadened $D2$ transition [10.9(0.5) GHz] [43], the ground state hyperfine structure interval (~6.8 GHz) [31], and the excited-state hyperfine structure frequency interval (~0.5 GHz) [42]. The large detuning does not affect the magnetic resonance significantly, since the resonance broadening measured using ODR does not show a significant linewidth contribution from the probe laser. A circularly polarized CW pump beam with 794.990(1)-nm wavelength in vacuum, 1.30(1)-mW optical power, and ~3-mm flat-top diameter also propagates along the axis of the vapor cell and prepares the atoms in the $|2, +2\rangle$ stretched state. The pump beam is resonant (detuning of $-0.2(5)$ GHz) with the pressure-broadened D_1 atomic transition in ^{87}Rb [see Fig. 1(A)] [43], [44]. The D_1 atomic transition's pressure broadening exceeds the ground state hyperfine interval, ensuring the effectiveness of the stretched state optical pumping process. A longitudinal field B_0 is applied along the direction of both laser beams.

The pump beam can be detected after the cell using a flip mirror and a slow-response photodetector (dc-PD, Thorlabs PDA 36A [45]). During the pump beam detection, the probe light is blocked before the vapor cell. The total pump optical power reaching the dc-PD photodetector is 0.45(1) mW. The dc-PD output is sent to a lock-in amplifier for phase-sensitive ODR detection.

For direct optical detection of the microwave signal, the probe beam is sent through a polarimeter—a high-quality Glan-Thomson polarizer oriented at 45(1)° with respect to the linear polarization of the probe beam. The probe light at the first polarimeter output is focused on a fast photodetector (Newport model 818-88-45 [45]) that detects the modulation of the probe optical power transmitted through the polarimeter resulting from its polarization rotation. This process can also be described in terms of parametric frequency conversion with the polarimeter allowing the detection of the optical beat note between the probe beam carrier and the orthogonally polarized sidebands generated by the coherently driven atomic medium [34]. The light of the second polarimeter output is discarded. The total probe optical power focused on the fast photodetector is 3.90(1) mW. The photodetector output in the vicinity of 6.8 GHz is sent to a spectrum analyzer (Agilent E4407B [45]) after amplification with a microwave amplifier (Minicircuits ZRON-8G+ [45]).

The polarimeter optical output is also used to perform detection of the time-averaged polarization rotation of the probe beam using a balanced photodetector (Newport Nirvana 2007 [45], 125-kHz bandwidth, not shown in Fig. 1). For the balanced detection measurements, the pump light is filtered out using a bandpass optical filter (Thorlabs FL05780-10 [45]). The balanced polarimeter measurements are discussed in the following in the context of ODR resonance measurements.

A microwave signal at a frequency in the vicinity of 6.8 GHz is sent to a small non-magnetic single-loop microwave antenna (~1.5 mm radius) positioned inside the magnetic shield, 16(1) mm away from the vapor cell. The signal is generated by a signal generator (HP 83 742 B [45]) frequency-referenced by the spectrum analyzer, allowing us to compare the generated and detected signal frequencies precisely. The plane of the

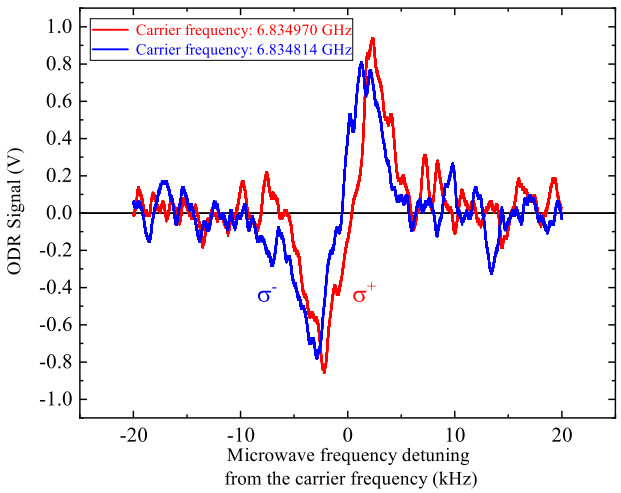

Fig. 2. Pump light absorption as a function of the microwave frequency detuning from the carrier frequency. (A) Carrier frequency 6.834970 GHz (red, σ^+ symbol). (B) Carrier frequency 6.834814 GHz (blue, σ^- symbol). The signal generator output power was −13.0(1.0) dBm.

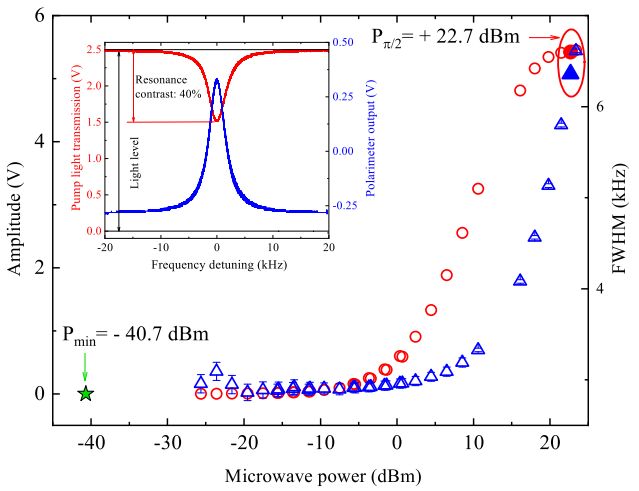

Fig. 3. Signal amplitude (red circles) and full-width at half-maximum (blue triangles) of the ODR resonance as a function of the microwave signal power delivered to the antenna loop. Inset: examples of ODR resonance measurement as a function of the microwave frequency detuning at the maximum power of 22.7(1.0) dBm using phase detection of the transmitted pump light (left scale) or polarimeter detection of the probe light (right scale). Star symbol: directly detected microwave signal at $P_{\min} = -40.7(1.0)$ dBm (see Section V).

antenna is parallel to the direction of the bias magnetic field B_0.

IV. Microwave-Optical Double Resonances—Pump Light Detection

Microwave-ODR measurements were performed by monitoring the absorption of the pump laser beam as a function of the microwave signal frequency. The flip mirror in Fig. 1(F) was used to deflect the σ^+ circularly polarized pump laser beam toward the dc-PD photodetector. The output of the photodetector was sent to a digital lock-in amplifier (Stanford Research Systems, SRS-830 [45], time constant 10 ms, and sensitivity 5 mV). The static magnetic field was set to ∼3.7 μT. The signal generator delivered −13.0(1.0)-dBm microwave power to the loop antenna. The microwave signal was frequency- modulated (FM) at 500-Hz rate with a modulation depth of 2 kHz with the carrier frequency scanned in 2 s over 40-kHz frequency span. The FM signal was also used as a reference for the lock-in amplifier. Measurements were performed at two values of the carrier frequency: 6.834970 and 6.834814 GHz. For the first frequency value, the magnetic field was oriented along the pump beam direction, while for the second frequency value, it was against the pump beam direction. The measured lock-in output as a function of the microwave carrier frequency is shown in Fig. 2.

The higher frequency resonance corresponds to the $|2, 2\rangle \longrightarrow |1, 1\rangle$ microwave transition, which has a higher frequency for $B_0 > 0$. The σ^+ circularly polarized pump laser prepares the atoms in the $|2, 2\rangle$ stretched state, leading to reduced pump beam absorption. The microwave field transfers atoms to the $|1, 1\rangle$ stretched state, leading to increased pump beam absorption. The lower frequency resonance corresponds to the $|2, -2\rangle \longrightarrow |1, -1\rangle$ microwave transition, as changing the orientation of B_0 leads to optical pumping in the opposite $|2, -2\rangle$ stretched state.

The difference between the resonant frequencies allows us to determine the magnetic field magnitude $B_0 = 3.7$ μT. The ODR resonance was measured as a function of microwave power delivered to the loop antenna. Again, a frequency span of 40 kHz in a 2-s time interval was used. The microwave signal was FM modulated at 400 Hz with 500-Hz modulation depth. The pump beam, detected with the dc-PD, was sent to the lock-in amplifier (10-ms time constant). The microwave power was changed between −25.6(1.0) and +22.7(1.0) dBm using a combination of attenuators as well as a microwave amplifier (Minicircuits ZRON-8G+ [45]). The microwave power was calibrated using a power meter (Agilent E4419B [45]). The signal amplitude and linewidth $\Delta\nu$ (full-width at half-maximum) as a function of the microwave power delivered to the microwave antenna loop were determined by the analysis of the recorded resonance spectra (see Fig. 2). The spectra were analyzed using a Lorentzian profile derivative as a fit function with offset, center frequency, amplitude, and linewidth $\Delta\nu$ used as fit parameters. The results are shown in Fig. 3.

The inset in Fig. 3 (left scale) shows the ODR resonance at maximum microwave power measured using phase detection of the transmitted pump laser power with the probe beam blocked before the vapor cell. The resonance shows 40% contrast or transmission change between on- and off-resonance. Fig. 3 (right scale) shows the ODR resonance using balanced polarimeter detection. For this measurement, the pump beam is blocked in front of the balanced photodetector with an interference filter. As noted earlier, when the microwave field frequency is off-resonance, the average polarization rotation angle is determined by atoms pumped mostly into the stretched $|2, +2\rangle$ state. On resonance, a significant portion of the atoms are in a superposition of the two $|2, +2\rangle$ and $|1, +1\rangle$ stretched states, changing the average polarization rotation angle and resulting in a resonance in the polarimeter output.

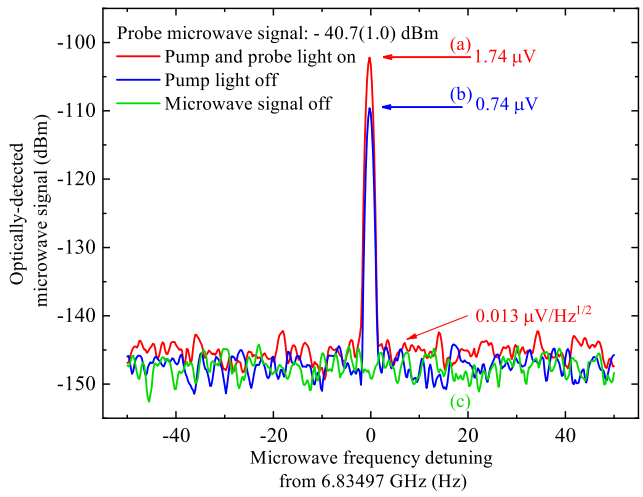

Fig. 4. Spectrum of the directly detected microwave signal as a function of the detuning of the microwave signal from 6.83497 GHz. (a) Pump and probe light ON. (b) Pump light OFF and probe light ON. (c) Microwave signal OFF. Note: both the optically detected signal and the microwave field signal are measured in dBm units and should not be confused.

V. Microwave-Optical Double Resonances—Probe Light Detection

As a second demonstration, the flip mirror was removed, and the probe beam was turned on. The microwave signal sent to the antenna loop had a fixed frequency of 6.834970 GHz and $P_{\min} = -40.7(1.0)$ dBm power. The output of the μw-PD photodetector was measured with the spectrum analyzer in 100-Hz frequency span and resolution bandwidth of 1 Hz. Three signals were measured: with both pump and probe beams present, with the pump beam blocked before the vapor cell, and with no light on the μw-PD. The results are shown in Fig. 4. The microwave power used for this measurement is also indicated with a star symbol in Fig. 3.

The measurements show that direct optical microwave detection has a higher sensitivity than the ODR method. Also, the microwave signal is detected directly and its phase is determined by the phase of the generated microwave field, as can be inferred by the instrument resolution-limited signal shown in Fig. 4. This is an important difference to the ODR detection technique. The phase relation between the generated microwave signal and the optically detected one was also demonstrated by heterodyne detection. The optically detected microwave signal at 6.834970 GHz was mixed with that of a stable 6.834971-GHz reference signal phase locked to the signal generator feeding the loop antenna. The microwave mixer output showed a beat-note signal at 1 kHz, having a phase related to the phase of the signal generator.

The measured signal-to-noise ratio SNR $\sim$ 1 μV/13 nV = 77, after removing the 0.74-μV signal picked up directly by the photodetector when the pump light is OFF [trace Fig. 4(b)], is significantly higher than the one for the microwave-ODR data seen in Fig. 2 that was measured at 28(1.4)-dB higher microwave power.

The value of the magnetic field component in the vapor cell can only be determined indirectly, as the microwave power distribution of the antenna loop field is not simulated. Appendices VII-C–VII-E discuss various ways to estimate the magnetic field sensitivities that are given in Table I. The results in Table I show that it is possible to reach a conservative limit of the sensitivity of 1.2(1.0) pT/Hz$^{1/2}$ or 3.7(3.1) μV/cm/Hz$^{1/2}$ in 33-mm^3 active volume. The sensitivity uncertainty is determined by the range of values given in Table I, columns 2 and 3. This limit is similar to the best achieved sensitivity of 3 μV/cm/Hz$^{1/2}$ using Rydberg atoms [46] in a 3000-mm^3 volume cell. The sensitivity limit corresponds to a Rabi frequency of $\sim$0.05 rad/s.

TABLE I

Microwave Sensor Sensitivity Parameters Estimated Using Section VII-C–VII-E. Column 2: Magnetic Field Component Sensitivity. Column 3: Electric Field Component Sensitivity. Column 4: Noise Floor Power Spectrum Density (PSD). Column 5: Microwave Photon Flux

Section	B-field sensitivity (pT/Hz$^{1/2}$)	E-field sensitivity (μV/cm/Hz$^{1/2}$)	Noise PSD (dBm/Hz)	Photon flux $\dot{n}$ (s^{-1})
VII-C	0.2	0.6	-132	1.4×10^7
VII-D	1.2	3.7	-117	4.9×10^8
VII-E	0.9	2.6	-119	2.5×10^8

The flux of microwave photons required to reach the measured sensor sensitivity is above 10^8/s [see Table I (last column)]. The relatively high photon flux required to reach the sensor noise floor is a result of the limited sensor bandwidth $\Delta\nu$ and the fact that the sensor is averaging the detected field. The sensor will detect a signal with SNR = 1 only after being exposed to the continuous flux of microwave photons for a time corresponding to $1/\Delta\nu$. To detect a microwave signal pulse above the sensor's noise floor, the pulse area given by the product of its Rabi frequency $\Omega_{R,\mu\mathrm{w}}(B)$ and duration τ must obey

$$\Omega_{R,\mu\mathrm{w}}(B)\tau > \Omega_{R,\mu\mathrm{w}}(B_{\mathrm{sens}})/\Delta\nu \tag{1}$$

where B_{sens} is the sensor's sensitivity given in Table I.

VI. Discussion

While the operation configuration of the microwave sensor shown in Fig. 1(C) is different from that of the generic RF atomic magnetometer shown in Fig. 1(B), a comparison between the two is useful with respect to the achievable sensitivity limits for the low-level microwave detection. As shown in Section VII-A, the microwave transition Rabi frequency $\Omega_{R,\mu\mathrm{w}}$ is a factor of $\sqrt{3}$ higher than the corresponding Zeeman transition Rabi frequency $\Omega_{R,Z}$ that is relevant to the RF magnetometer. An RF magnetometer using a vapor cell with a similar volume of 27 mm^3 demonstrated a magnetic resonance linewidth of 1 kHz and a noise floor of 0.16(1) pT/Hz$^{1/2}$ [47]. Assuming similar pump and probe intensities and detection efficiency, the expected microwave field noise floor of the microwave sensor used in this paper would be $\sim 0.16(1)/\sqrt{3}$ pT/Hz$^{1/2}$ = 0.09(5) pT/Hz$^{1/2}$, corresponding to 0.28(0.2) μV/cm/Hz$^{1/2}$, below the estimations shown in Table I.

The best demonstrated RF magnetometer sensitivity is $\sim$1 fT/Hz$^{1/2}$ in a cubic centimeter [22]. Assuming the same performance could be reached for microwave sensors, this would correspond to an electric field sensitivity of 6 nV/cm/Hz$^{1/2}$ or to direct detection of a traveling-wave microwave power of -163 dBm propagating through 1-cm^2 cross section of the 1-cm^3 active volume. Achieving such performance will depend on the uniformity and noise properties of the optical fields and the bias magnetic field that influence the parametric conversion process, as well the detection efficiency and noise.

It is important to point out that this paper explores a parametric process that leads to microwave-to-optical transduction on a one-to-one basis [35]. Also, the employed separation of the pump and probe processes allows their independent optimization. The sensor is based on two experimental techniques—optical pumping into a stretched atomic state and detection of an off-resonant probe beam—that have been successfully used in room-temperature experiments to suppress the spin-exchange rate [48], to store light and create single-photon memory [49], [50], to improve the sensitivity of an RF magnetometer using entanglement [51], and to entangle a record number of atoms [52].

VII. Estimation of Microwave Field Amplitude at the Sensor Position

A. Zeeman Versus Microwave Transitions

In this section, the transition matrix elements and frequency separation between atomic states involved in RF and microwave-frequency detection are given. The interaction Hamiltonian due to the ac magnetic field signal is

$$H_B(t) = \sum_{k=x,y,z} \mu_B B_k(t)(g_I I_k + g_J J_k) \tag{2}$$

where μ_B is the Bohr magneton and $\mathbf{I}$ and $\mathbf{J}$ are the total nuclear angular momentum and the total electron angular momentum operators.

Atomic transitions that cause a change of the total angular momentum projection $\Delta m_F = \pm 1$ are due to ac signals with magnetic component orthogonal to the quantization axis. A linearly polarized field with magnetic component $\vec{B}(t) = B_x(t)$ is considered. For the case of Fig. 1(B), the relevant transition in ^{87}Rb is $|2,2\rangle \longrightarrow |2,1\rangle$, while for the case of Fig. 1(C), the transition is $|2,2\rangle \longrightarrow |1,1\rangle$. The angular and Rabi frequencies of the corresponding transitions are

$$\begin{aligned}
\omega_{2,2} - \omega_{1,1} &= \omega_{\mathrm{HFS}} + \frac{(3g_J + g_I)\mu_B}{4\hbar} B_0 \\
\omega_{2,2} - \omega_{2,1} &= \frac{(g_J + 3g_I)\mu_B}{4\hbar} B_0 \\
\Omega_{R,\mu\mathrm{w}} &= \frac{\sqrt{3}}{8\hbar}(g_J - g_I)\mu_B B_x(t) \\
\Omega_{R,\mathrm{Z}} &= \frac{1}{8\hbar}(g_J + 3g_I)\mu_B B_x(t)
\end{aligned} \tag{3}$$

where g_J and g_I are the Landé factor and the nuclear g-factor [53], $\nu_0 = 6.835$ GHz, and B_0 is the static bias magnetic field value. Since $g_I \approx 10^{-3} g_J$, it can be neglected, resulting in a matrix element ratio of $\sqrt{3}$.

B. Poynting Vector and Microwave Photon Flux

The average energy density u_B of an electromagnetic field with a magnetic field component B in vacuum is

$$u_B = \frac{1}{2\mu_0} B^2 = \frac{1}{c}\langle S \rangle \tag{4}$$

where μ_0 is the magnetic constant, $\langle S \rangle$ is the time-averaged amplitude of the directional energy flux (the Poynting vector) of an electromagnetic field in vacuum, and c is the speed of light. An energy density equivalent to a single microwave photon of frequency $\nu_0 = 6.835$ GHz in the vapor cell volume of 33 mm^3 corresponds to 19-pT microwave field magnetic component.

The magnetic component of a directional energy flux of microwave photons arriving at a rate of $\dot{n}$ across the area A is

$$B = \sqrt{\frac{2\mu_0}{c}\langle S \rangle} = \sqrt{\frac{2\mu_0}{c}\frac{2\pi\hbar\nu_0\dot{n}}{A}}. \tag{5}$$

C. Estimation of the Detected Magnetic Component Amplitude—Loop Antenna

The magnetic field component of the microwave field reaching the vapor cell can be estimated considering near-field regime. The microwave antenna loop has a radius of $r \sim 1.5$ mm and is placed $d = 16(1)$ mm away from the vapor cell. The near-field regime estimation is justified because both these dimensions are smaller than the 43-mm wavelength of the 6.8-GHz microwave signal. The directly detected microwave signal shown in Fig. 4 was obtained with microwave power $P_{\min} = -40.7(1.0)$ dBm delivered to the microwave antenna by the $R = 50\ \Omega$ output impedance signal generator that generated an ac current $i = (P_{\min}/R)^{1/2}$ in the loop. The magnetic field caused by this current at a distance d from the loop along the loop axis is

$$B_{\min} = \frac{\mu_0 r^2 \sqrt{P_{\min}/R}}{2(d^2 + r^2)^{3/2}} \tag{6}$$

resulting in a magnetic field amplitude of 14 pT, measured with SNR $\sim$ 77. The estimated measurement sensitivity and other relevant parameters are given in the second row of Table I.

D. Estimation of the Detected Magnetic Component Amplitude—Tipping Angle

The two $|2,2\rangle$ and $|1,1\rangle$ stretched atomic states can be represented as the two poles of the Bloch sphere. The optical pumping process prepares the atomic system in the initial $|2,2\rangle$ state, with the Bloch vector aligned with the vertical axis. The microwave interaction rotates the Bloch vector away from the axis. The tipping angle related to the microwave interaction is estimated in the following. The Rabi frequency of the interaction is determined by the magnetic component of the microwave field and the corresponding Rabi frequency given by (3).

From the ODR measurements shown in Fig. 3, the resonance linewidth at zero microwave power is $\Delta\nu = 2.9(1)$ kHz, limited by the decoherence time $T_2 = 1/\Delta\nu$. It is assumed that the tipping angle $\theta_{\pi/2} = \Omega_R \times T_2 = \pi/2$ corresponding to the

maximum signal sensitivity is determined by T_2. An estimation for the magnetic component of the microwave field can thus be obtained from the expression

$$B_{\pi/2} = \frac{4\pi\hbar\Delta\nu}{\sqrt{3}(g_J - g_I)\mu_B}. \tag{7}$$

Equation (7) results in a magnetic component magnitude of $B_{\pi/2} = 119$ nT. The maximum signal amplitude (at tipping angle $\theta_{\pi/2}$) was detected at a microwave power $P_{\pi/2} = +22.7(1.0)$ dBm. The optically detected microwave signal shown in Fig. 4 was measured at a microwave power $P_{\min} = -40.7(1.0)$ dBm, resulting in a corresponding magnetic component amplitude of 81 pT, measured with SNR $\sim$ 77. The estimated measurement sensitivity and other relevant parameters are given in the third row of Table I.

E. Estimation of the Detected Magnetic Component Amplitude—Resonance Broadening

The amplitude of the magnetic component of the microwave field at maximum ODR signal can be estimated from the observed ODR resonance broadening. A simple Bloch picture model predicts a broadened linewidth $\Delta\nu'$

$$\Delta\nu' = \frac{1}{T_2}\sqrt{1 + \left(\frac{(3g_J + g_I)\mu_B}{8\hbar}T_2 B\right)^2} = \sqrt{\Delta\nu^2 + \left(\frac{(3g_J + g_I)\mu_B}{8\hbar}B\right)^2}. \tag{8}$$

Using the resonance's magnetic field sensitivity given by 3, a low-power resonance linewidth limit $\Delta\nu = 2.9(1)$ kHz, and a power-broadened linewidth of $\Delta\nu' = 6.36(1)$ kHz at $P_{\pi/2} = 22.7(1.0)$ dBm microwave power, the resonance broadening expression can be used to estimate the magnetic-component amplitude of the microwave field

$$B_\Delta = \frac{8\hbar\sqrt{\Delta\nu'^2 - \Delta\nu^2}}{(3g_J + g_I)\mu_B} \tag{9}$$

resulting in $B_\Delta = 85.7$ nT. The optically detected microwave signal shown in Fig. 4 was measured at a microwave power $P_{\min} = -40.7(1.0)$ dBm, resulting in a detected magnetic component of 58 pT, measured with SNR $\sim$ 77. The estimated measurement sensitivity and other relevant parameters are given in the fourth row of Table I.

F. Magnetic Component Amplitude of the Room-Temperature Thermal Background Radiation at 6.835 GHz

The total thermal electromagnetic energy density at absolute temperature T in a frequency interval ν, $\nu + d\nu$ according to Planck's law of thermal radiation is

$$\rho(\nu)d\nu = \frac{8\pi\nu^2}{c^3}\frac{2\pi\hbar\nu}{e^{2\pi\hbar\nu/k_BT} - 1}d\nu. \tag{10}$$

The atomic system is sensitive in a narrow spectral range $\Delta\nu = 2.9$ kHz in the vicinity of $\nu_0 = 6.8$ GHz. Over this range, the variation of the exponent in the expression above can be ignored. For simplicity, the frequency response of the atomic system within the $\Delta\nu$ spectral range can be assumed constant. The resulting electromagnetic energy density is

$$u_T = \frac{16\pi^2\hbar\nu_0^3}{c^3}\frac{\Delta\nu}{e^{2\pi\hbar\nu_0/k_BT} - 1}. \tag{11}$$

Using 4, the corresponding average magnetic component of the thermal radiation in a frequency interval $\Delta\nu$ centered at ν_0 is

$$B_T = \sqrt{\frac{32\pi^2\mu_0\hbar\nu_0^3\Delta\nu}{c^3(e^{2\pi\hbar\nu_0/k_BT} - 1)}}. \tag{12}$$

This value corresponds to $B_T = 36$ fT at room temperature ($T = 300$ K) in a $\Delta\nu = 2.9$ kHz bandwidth and to 0.67 fT in 1-Hz bandwidth.

The thermal radiation background at room temperature in 1-Hz bandwidth in the vapor cell volume corresponds to 1.3×10^{-9} photons. For comparison, the Nyquist–Johnson noise in 1-Hz bandwidth in a room-temperature conductor is $k_BT/2\pi\hbar\nu_0 = 915$ photons, with k_B Boltzmann's constant. The difference in the photon numbers shows the advantage of detecting microwave signals in three dimensions.

VIII. Conclusion

The results of this paper show that it is possible to directly detect the magnetic component amplitude of weak microwave signals in the gigahertz range using a simple setup based on a buffer-gas vapor cell. The amplitude detection allows access to the phase of the microwave field and the use of phase demodulation schemes at the microwave frequency. The demonstrated sensitivity is below 1.2(1.0) pT/Hz$^{1/2}$ (magnetic field component) or 3.7(3.1) μV/cm/Hz$^{1/2}$ (electric field component). The detected microwave frequency is in the vicinity of 6.835 GHz, but is tunable at 21-kHz/μT rate by changing the value of the static magnetic field B_0. At the same time, the frequency tunability range will be limited by the inhomogeneity and noise of the bias magnetic field that would lead to a resonance broadening even before the Paschen–Back regime is reached. The results obtained using a ^{87}Rb buffer gas vapor cell of 33-mm^3 internal volume are similar to the sensitivity limit achieved with Rydberg atoms-based sensors. A further increase of sensitivity is expected using optimized vapor cell parameters, spectroscopy parameters, and optical detection.

Acknowledgment

This work is a contribution of the National Institute of Standards and Technology (NIST), an agency of the U.S. Government, and is not subject to copyright in USA. The authors would like to thank Dr. D. Howe for the helpful discussions, and Dr. C. Holloway and Dr. D. Leibfried for careful reading of this paper's manuscript.

References

[1] T. L. Nicholson *et al.*, "Systematic evaluation of an atomic clock at 2×10^{-18} total uncertainty," *Nat. Commun.*, vol. 6, pp. 1–8, Apr. 2015, Art. no. 6896. doi: 10.1038/ncomms7896.

[2] N. Huntemann, C. Sanner, B. Lipphardt, C. Tamm, and E. Peik, "Single-ion atomic clock with 3×10^{-18} systematic uncertainty," *Phys. Rev. Lett.*, vol. 116, no. 6, 2016, Art. no. 063001.

[3] W. F. McGrew *et al*, "Atomic clock performance enabling geodesy below the centimetre level," *Nature*, vol. 564, pp. 87–90, Nov. 2018. doi: 10.1038/s41586-018-0738-2.

[4] D. Sheng, S. Li, N. Dural, and M. V. Romalis, "Subfemtotesla scalar atomic magnetometry using multipass cells," *Phys. Rev. Lett.*, vol. 110, pp. 160802-1–160802-5, Apr. 2013.

[5] S.-K. Lee, K. L. Sauer, S. J. Seltzer, O. Alem, and M. V. Romalis, "Subfemtotesla radio-frequency atomic magnetometer for detection of nuclear quadrupole resonance," *Appl. Phys. Lett.*, vol. 89, no. 21, 2006, Art. no. 214106. doi: 10.1063/1.2390643.

[6] H. Fan, S. Kumar, J. Sedlacek, H. Kübler, S. Karimkashi, and J. P. Shaffer, "Atom based RF electric field sensing," *J. Phys. B, At. Mol. Opt. Phys.*, vol. 48, no. 20, 2015, Art. no. 202001. [Online]. Available: http://stacks.iop.org/0953-4075/48/i=20/a=202001

[7] J. A. Sedlacek, A. Schwettmann, H. Kübler, R. Low, T. Pfau, and J. P. Shaffer, "Microwave electrometry with Rydberg atoms in a vapour cell using bright atomic resonances," *Nat. Phys.*, vol. 8, no. 11, pp. 819–824, Sep. 2012. doi: 10.1038/nphys2423.

[8] C. L. Holloway, M. T. Simons, J. A. Gordon, A. Dienstfrey, D. A. Anderson, and G. Raithel, "Electric field metrology for SI traceability: Systematic measurement uncertainties in electromagnetically induced transparency in atomic vapor," *J. Appl. Phys.*, vol. 121, no. 23, Jun. 2017, Art. no. 233106. doi: 10.1063/1.4984201.

[9] H. Q. Fan, S. Kumar, R. Daschner, H. Kübler, and J. P. Shaffer, "Subwavelength microwave electric-field imaging using Rydberg atoms inside atomic vapor cells," *Opt. Lett.*, vol. 39, no. 10, pp. 3030–3033, May 2014. [Online]. Available: http://ol.osa.org/abstract.cfm?URI=ol-39-10-3030

[10] C. L. Holloway *et al*, "Sub-wavelength imaging and field mapping via electromagnetically induced transparency and Autler-Townes splitting in Rydberg atoms," *Appl. Phys. Lett.*, vol. 104, no. 24, 2014, Art. no. 244102. doi: 10.1063/1.4883635.

[11] C. L. Holloway, M. T. Simons, M. D. Kautz, A. H. Haddab, J. A. Gordon, and T. P. Crowley, "A quantum-based power standard: Using Rydberg atoms for a SI-traceable radio-frequency power measurement technique in rectangular waveguides," *Appl. Phys. Lett.*, vol. 113, no. 9, 2018, Art. no. 094101. doi: 10.1063/1.5045212.

[12] T. P. Crowley, E. A. Donley, and T. P. Heavner, "Quantum-based microwave power measurements: Proof-of-concept experiment," *Rev. Sci. Instrum.*, vol. 75, no. 8, pp. 2575–2580, Aug. 2004.

[13] A. Horsley, G.-X. Du, M. Pellaton, C. Affolderbach, G. Mileti, and P. Treutlein, "Imaging of relaxation times and microwave field strength in a microfabricated vapor cell," *Phys. Rev. A, Gen. Phys.*, vol. 88, Dec. 2013, Art. no. 063407. doi: 10.1103/PhysRevA.88.063407.

[14] A. Affolderbach, G.-X. Du, T. Bandi, A. Horsley, P. Treutlein, and G. Mileti, "Imaging microwave and DC magnetic fields in a vapor-cell Rb atomic clock," *IEEE Trans. Instrum. Meas.*, vol. 64, no. 12, pp. 3629–3637, Dec. 2015. doi: 10.1109/TIM.2015.2444261.

[15] A. Horsley, P. Du, and G.-X. Treutlein, "Widefield microwave imaging in alkali vapor cells with sub-100 μm resolution," *New J. Phys.*, vol. 17, no. 11, 2015, Art. no. 112002. [Online]. Available: http://stacks.iop.org/1367-2630/17/i=11/a=112002

[16] A. Horsley and P. Treutlein, "Frequency-tunable microwave field detection in an atomic vapor cell," *Appl. Phys. Lett.*, vol. 108, no. 21, May 2016, Art. no. 211102.

[17] M. Kinoshita and M. Ishii, "Measurement of microwave magnetic field in free space using the Rabi frequency," in *IEEE CPEM Conf. Dig.*, Jul. 2016, pp. 1–2.

[18] F. Sun, J. Ma, Q. Bai, X. Huang, B. Gao, and D. Hou, "Measuring microwave cavity response using atomic Rabi resonances," *Appl. Phys. Lett.*, vol. 111, no. 5, pp. 1–5, Aug. 2017, Art. no. 051103.

[19] S. Hao, J. Ma, X. Li, J. Liu, C. Li, and S. Zhang, "A quantum-based microwave magnetic field sensor," *Sensors*, vol. 18, no. 10, p. 3288, 2018. [Online]. Available: http://www.mdpi.com/1424-8220/18/10/3288

[20] J. Vanier and C. Audoin, *The Quantum Physics of Atomic Frequency Standards*. Bristol, U.K.: IOP Publishing, 1989.

[21] J. C. Camparo, "Atomic stabilization of electromagnetic field strength using Rabi resonances," *Phys. Rev. Lett.*, vol. 80, no. 2, pp. 222–225, Jan. 1998.

[22] I. M. Savukov, S. J. Seltzer, M. V. Romalis, and K. L. Sauer, "Tunable atomic magnetometer for detection of radio-frequency magnetic fields," *Phys. Rev. Lett.*, vol. 95, Aug. 2005, Art. no. 063004. doi: 10.1103/PhysRevLett.95.063004.

[23] A. H. Firester and T. R. Carver, "Intensity modulation of transmitted light at the ground-state hyperfine frequency of K^{39}," *Phys. Rev.*, vol. 164, pp. 76–83, Dec. 1967. doi: 10.1103/PhysRev.164.76.

[24] B. S. Mathur, H. Tang, R. Bulos, and W. Happer, "Microwave light modulation by an optically pumped Rb^{87} vapor," *Phys. Rev. Lett.*, vol. 21, pp. 1035–1038, Oct. 1968. doi: 10.1103/PhysRevLett.21.1035.

[25] M. Kiffner, K. T. Feizpour, A. Kaczmarek, D. Jaksch, and J. Nunn, "Two-way interconversion of millimeter-wave and optical fields in Rydberg gases," *New J. Phys.*, vol. 18, no. 9, 2016, Art. no. 093030. [Online]. Available: http://stacks.iop.org/1367-2630/18/i=9/a=093030

[26] J. Han, T. Vogt, C. Gross, D. Jaksch, M. Kiffner, and W. Li, "Coherent microwave-to-optical conversion via six-wave mixing in Rydberg atoms," *Phys. Rev. Lett.*, vol. 120, Mar. 2018, Art. no. 093201. doi: 10.1103/PhysRevLett.120.093201.

[27] C. L. Holloway *et al*, "Atom-based RF electric field metrology: From self-calibrated measurements to subwavelength and near-field imaging," *IEEE Trans. Electromagn. Compat.*, vol. 59, no. 2, pp. 717–728, Apr. 2017.

[28] V. Gerginov, F. C. S. da Silva, and D. Howe, "Prospects for magnetic field communications and location using quantum sensors," *Rev. Sci. Instrum.*, vol. 88, no. 12, 2017, Art. no. 125005. doi: 10.1063/1.5003821.

[29] D. H. Meyer, K. C. Cox, F. K. Fatemi, and P. D. Kunz, "Digital communication with Rydberg atoms and amplitude-modulated microwave fields," *Appl. Phys. Lett.*, vol. 112, no. 21, 2018, Art. no. 211108. doi: 10.1063/1.5028357.

[30] L. A. Williamson, Y.-H. Chen, and J. J. Longdell, "Magneto-optic modulator with unit quantum efficiency," *Phys. Rev. Lett.*, vol. 113, Nov. 2014, Art. no. 203601. doi: 10.1103/PhysRevLett.113.203601.

[31] F. Riehle, P. Gill, F. Arias, and L. Robertsson, "The CIPM list of recommended frequency standard values: Guidelines and procedures," *Metrologia*, vol. 55, no. 2, pp. 188–200, 2018. [Online]. Available: http://stacks.iop.org/0026-1394/55/i=2/a=188

[32] D. Budker, W. Gawlik, D. F. Kimball, S. M. Rochester, V. V. Yashchuk, and A. Weis, "Resonant nonlinear magneto-optical effects in atoms," *Rev. Mod. Phys.*, vol. 74, no. 4, pp. 1153–1201, Oct. 2002.

[33] W. Happer and B. S. Mathur, "Effective operator formalism in optical pumping," *Phys. Rev.*, vol. 163, no. 1, pp. 12–25, Nov. 1967.

[34] H. Tang and W. Happer, "Parametric frequency conversion of resonance radiation in optically pumped rubidium-87 vapor," *Phys. Rev. Lett.*, vol. 24, pp. 551–554, Mar. 1970. doi: 10.1103/PhysRevLett.24.551.

[35] H. Tang and W. Happer, "An optically pumped parametric frequency converter," in *Proc. 24th Annu. Symp. Freq. Control*, Apr. 1970, pp. 285–293.

[36] N. Cyr, M. Tetu, and M. Breton, "All-optical microwave frequency standard: A proposal," *IEEE Trans. Instrum. Meas.*, vol. 42, no. 2, pp. 640–649, Apr. 1993.

[37] M. Zhu, "High contrast signal in a coherent population trapping based atomic frequency standard application," in *Proc. IEEE Int. Freq. Control Symp.*, May 2003, pp. 16–21.

[38] A. Nagel *et al.*, "Experimental realization of coherent dark-state magnetometers," *Europhys. Lett.*, vol. 44, no. 1, p. 31, 1998. [Online]. Available: http://stacks.iop.org/0295-5075/44/i=1/a=031

[39] E. B. Aleksandrov, A. K. Vershovskii, and A. S. Pazgalev, "Magnetometer based on a pair of symmetric transitions in the ^{87}Rb hyperfine structure," *Tech. Phys.*, vol. 51, no. 7, pp. 919–923, 2006. doi: 10.1134/S1063784206070176.

[40] V. Shah, "System and method for measuring a magnetic gradient field," U.S. Patent 10 088 535 B1, Oct. 2, 2018.

[41] V. Gerginov, S. Krzyzewski, and S. Knappe, "Pulsed operation of a miniature scalar optically pumped magnetometer," *J. Opt. Soc. Amer. B, Opt. Phys.*, vol. 34, no. 7, pp. 1429–1434, 2017.

[42] J. Ye, S. Swartz, P. Jungner, and J. L. Hall, "Hyperfine structure and absolute frequency of the ^{87}Rb $5P_{3/2}$ state," *Opt. Lett.*, vol. 21, no. 16, pp. 1280–1282, Aug. 1996. [Online]. Available: http://ol.osa.org/abstract.cfm?URI=ol-21-16-1280

[43] M. V. Romalis, E. Miron, and G. D. Cates, "Pressure broadening of Rb D_1 and D_2 lines by ^{3}He, ^{4}He, N_2, and Xe: Line cores and near wings," *Phys. Rev. A, Gen. Phys.*, vol. 56, no. 6, pp. 4569–4578, Dec. 1997.

[44] M. Maric, J. J. McFerran, and A. N. Luiten, "Frequency-comb spectroscopy of the D_1 line in laser-cooled rubidium," *Phys. Rev. A, Gen. Phys.*, vol. 77, Mar. 2008, Art. no. 032502. doi: 10.1103/PhysRevA.77.032502.

[45] *Any Mention of Commercial Products is for Information Only*, NIST, Gaithersburg, MD, USA, 2018.

[46] S. Kumar, H. Fan, H. Kübler, J. Sheng, and J. P. Shaffer, "Atom-based sensing of weak radio frequency electric fields using homodyne readout," *Sci. Rep.*, vol. 7, pp. 1–10, Feb. 2017, Art. no. 42981. doi: 10.1038/srep42981.

[47] V. Gerginov, "Field-polarization sensitivity in RF atomic magnetometers," *Phys. Rev. Appl.*, vol. 11, Feb. 2019, Art. no. 024008. doi: 10.1103/PhysRevApplied.11.024008.
[48] S. Appelt, A. B.-A. Baranga, A. Young, and W. Happer, "Light narrowing of rubidium magnetic-resonance lines in high-pressure optical-pumping cells," *Phys. Rev. A, Gen. Phys.*, vol. 59, pp. 2078–2084, Mar. 1999. doi: 10.1103/PhysRevA.59.2078.
[49] C. Kupchak, T. Mittiga, B. Jordaan, M. Namazi, C. Nölleke, and E. Figueroa, "Room-temperature single-photon level memory for polarization states," *Sci. Rep.*, vol. 5, Jan. 2015, pp. 1–5, Art. no. 7658. doi: 10.1038/srep07658.
[50] O. Katz and O. Firstenberg, "Light storage for one second in room-temperature alkali vapor," *Nat. Commun.*, vol. 9, no. 1, pp. 1–6, 2018, Art. no. 2074. doi: 10.1038/s41467-018-04458-4.
[51] W. Wasilewski, K. Jensen, H. Krauter, J. J. Renema, M. V. Balabas, and E. S. Polzik, "Quantum noise limited and entanglement-assisted magnetometry," *Phys. Rev. Lett.*, vol. 104, Mar. 2010, Art. no. 133601. doi: 10.1103/PhysRevLett.104.133601.
[52] J. Kong R. Jiménez-Martíínez, C. Troullinou, V. G. Lucivero, and M. W. Mitchell, "Measurement-induced nonlocal entanglement in a hot, strongly-interacting atomic system," 2018, *arXiv:1804.07818*. [Online]. Available: https://arxiv.org/abs/1804.07818
[53] E. Arimondo, M. Iguscio, and P. Violino, "Experimental determination of hyperfine-structure in alkali atoms," *Rev. Mod. Phys.*, vol. 49, no. 1, pp. 31–75, 1977.

Vladislav Gerginov received the M.Sc. degree from Sofia University "St. Kliment Ohridski," Sofia, Bulgaria, in 1995, and the Ph.D. degree from the University of Notre Dame, Notre Dame, IN, USA, in 2003.

He was with the National Institute of Standards and Technology, Boulder, CO, USA, from 2002 to 2006, where he was involved in direct femtosecond comb spectroscopy, a photonic magnetometer project, and NIST's chip-scale atomic clock (CSAC) program awarded with the Department of Commerce's Silver Medal. From 2008 to 2016, he was a Staff Scientist with the National Metrology Institute of Germany (PTB). In 2016, he joined NIST and the University of Colorado at Boulder, as a Senior Research Associate, where he is currently involved in the development of optical references with improved stability and highly sensitive quantum sensors. His current research interests include precision spectroscopy, atomic clocks, and atomic magnetometry.

Fabio C. S. da Silva (M'05) received the B.Sc. and M.Sc. degrees in physics from the Federal University of Pernambuco, Recife, Brazil, in 1992 and 1995, respectively, and the Ph.D. degree in physics from the State University of Campinas, Campinas, Brazil, in 2000, and the M.B.A. degree in business from the University of Colorado at Boulder, Boulder, CO, USA, in 2010.

Since 2000, he has been involved in magnetic metrology with the National Institute of Standards and Technology (NIST), Boulder, where he has been developing an award-winning 256-channel magnetic scanner for forensic evidence validation delivered to the Federal Bureau of Investigation in 2007. He joined NIST as a Staff Scientist in 2016 and has focused his recent research on indoor localization and imaging.

Archita Hati (M'12) received the M.Sc. degree in physics, the M.Phil. degree in microwaves, and the Ph.D. degree in physics from the University of Burdwan, Bardhaman, India, in 1992, 1993, and 2001, respectively.

She is currently an Electronics Engineer with the Time and Frequency Division, National Institute of Standards and Technology, Boulder, CO, USA, where she is the Calibration Service Leader of the Time and Frequency Metrology Group. Her current research interests include phase noise metrology, ultra-low noise frequency synthesis, development of low-noise microwave and opto-electronic oscillators, and vibration analysis.

Dr. Hati was the recipient of the Allen V. Astin Measurement Science Award in 2015.

Craig Nelson (M'86) received the B.S.E.E. degree in electrical engineering from the University of Colorado at Boulder, Boulder, CO, USA, in 1990.

He is currently an Electrical Engineer with the Time and Frequency Division, National Institute of Standards and Technology (NIST), Boulder. He has authored over 70 papers and teaches classes, tutorials, and workshops at NIST, the IEEE Frequency Control Symposium, and several sponsoring agencies on the practical aspects of high-resolution phase noise metrology.

Mr. Nelson was the recipient of the NIST Bronze Medal in 2012 and the Allen V. Astin Measurement Science Award in 2015 for developing a world-leading program of research and measurement services in phase noise.